Structural and magnetic study of zinc-doped magnetite nanoparticles and ferrofluids for hyperthermia applications

2013 J. Phys. D: Appl. Phys. 46 125006

(http://iopscience.iop.org/0022-3727/46/12/125006)

J. Phys. D: Appl. Phys. **46** (2013) 125006 (12pp) doi:10.1088/0022-3727/46/12/125006

Structural and magnetic study of zinc-doped magnetite nanoparticles and ferrofluids for hyperthermia applications

P Mendoza Zélis[1], G A Pasquevich[1], S J Stewart[1], M B Fernández van Raap[1], J Aphesteguy[2], I J Bruvera[1], C Laborde[1], B Pianciola[1], S Jacobo[2,3] and F H Sánchez[1,3]

[1] IFLP-CONICET, CCT-La Plata and Departamento de Física, Facultad de Ciencias Exactas, Universidad Nacional de La Plata, CC 67, 1900 La Plata, Argentina
[2] INTECIN-CONICET and Departamento de Química, Facultad de Ingeniería, Universidad de Buenos Aires, Av. Paseo Colón 850, C1063ACV Buenos Aires, Argentina

E-mail: sanchez@fisica.unlp.edu.ar and sjacobo@fi.uba.ar

Received 11 October 2012, in final form 7 January 2013
Published 25 February 2013
Online at stacks.iop.org/JPhysD/46/125006

Abstract
Cubic-like shaped $Zn_xFe_{3-x}O_4$ particles with crystallite mean sizes D between 15 and 117 nm were obtained by co-precipitation. Particle size effects and preferential occupation of spinel tetrahedral site by Zn^{2+} ions led to noticeable changes of physical properties. $D \geqslant 30$ nm particles displayed nearly bulk properties, which were dominated by Zn concentration. For $D \leqslant 30$ nm, dominant magnetic relaxation effects were observed by Mössbauer spectroscopy, with the mean blocking size $D_B \sim 13$ to 15 nm. Saturation magnetization increased with x up to $x \sim 0.1$–0.3 and decreased for larger x. Power absorbed by water and chitosan-based ferrofluids from a 260 kHz radio frequency field was measured as a function of x, field amplitude H_0 and ferrofluid concentration. For $H_0 = 41$ kA m^{-1} the maximum specific absorption rate was 367 W g^{-1} for $D = 16$ nm and $x = 0.1$. Absorption results are interpreted within the framework of the linear response theory for $H_0 \leqslant 41$ kA m^{-1}. A departure towards a saturation regime was observed for higher fields. Simulations based on a two-level description of nanoparticle magnetic moment relaxation qualitatively agree with these observations. The frequency factor of the susceptibility dissipative component, derived from experimental results, showed a sharp maximum at $D \sim 16$ nm. This behaviour was satisfactorily described by simulations based on moment relaxation processes, which furthermore indicated a crossover from Néel to Brown mechanisms at $D \sim 18$ nm. Hints for further improvement of magnetite particles as nanocalefactors for magnetic hyperthermia are discussed.

S Online supplementary data available from stacks.iop.org/JPhysD/46/125006/mmedia

(Some figures may appear in colour only in the online journal)

1. Introduction

Magnetic nanoparticles (MNPs) are used in biomedical trials for several diagnosis and therapy applications (Pankhurst *et al* 2009). Magnetic hyperthermia therapy appears a promising technique for low invasive treatment of tumours, alone or by improving the efficiency of chemo (Ren *et al* 2012), radio (Maier-Hauff *et al* 2011) and photodynamic therapies (de Paula *et al* 2012). A relatively small increase in temperature of 5–8 °C produces a large effect on cancer cell viability (Overggard 1989). Magnetic hyperthermia therapy is currently performed in clinical tries by exposing nanoparticles internalized into tumours to a radio frequency (RF) field with an amplitude of about 1×10^4 to 2.5×10^4 A m^{-1} (Gneveckow *et al* 2004, Maier-Hauff *et al* 2011). Single domain MNPs absorb power from the field through magnetic relaxation processes

[3] Authors to whom any correspondence should be addressed.

and dissipate it into the tumour increasing its temperature, leading to the apoptosis of the tumour cells. The power delivered by MNPs can be varied by changing magnetic field amplitude (H_0) and frequency (f), but these quantities cannot exceed physiologically imposed limits. It has been reported that parts of the human body with a mean diameter of 0.3 m cannot be exposed without discomfort to RF fields for which the product fH_0 is larger than 5×10^8 A ms^{-1} (Brezovich 1987). However, there is a need for new independent determinations of the discomfort factor and also for a general discussion on its definition. It seems reasonable that its value should depend on the particular clinical case as well as on specific treatment variables such as field localization and length of on/off periods. Nevertheless, due to the existence of a discomfort threshold, the enhancement of delivered power relies on MNPs performance improvement. For this improvement biocompatibility and toxicity requirements must be fulfilled (Häfeli *et al* 2007). The best candidate for hyperthermia treatments should be a biocompatible magnetic material displaying large saturation magnetization (M_s) and a Curie temperature (T_c) just above the therapeutic one of 42–45 °C. The latter provides a convenient heating off switch, preventing hazardous overheating.

Ferrimagnetic iron oxides have the largest M_s of all known biocompatible materials and are low cost. Although their ordering temperature is well above the therapeutic one, they are the most preferred materials for magnetic hyperthermia. Magnetite Fe_3O_4 has an ordering temperature of $T_N = 860$ K (Smith 1956) and a room temperature (RT) $M_s = 90$ A m^2 kg^{-1} (Chikazumi 1964) . This compound has a cubic inverse spinel structure where two thirds of the iron ions are Fe^{3+}, half of these occupy A sites (tetrahedral sites) and the other half occupy B sites (octahedral sites). The remaining Fe ions are Fe^{2+} and occupy B sites.

Doping magnetite with transition metal elements allows the modification of quantities such as M_s. Here Zn-doped magnetite is studied as a first step of a project which foresees further improvement using other additives (Tasaki and Izushi 1977, Behdadfar *et al* 2012). $Zn_xFe_{3-x}O_4$ ($0 \leqslant x \leqslant 0.5$) MNPs and their aqueous ferrofluids (FF) were prepared by chemical co-precipitation synthesis route. This relatively inexpensive preparation technique was selected considering that therapeutic applications for the general public demand low cost materials. Mean MNP sizes and compositions were selected within a wide range of values in order to identify material parameters intervals in which high specific absorption rates (SARs) can be obtained (Hergt *et al* 2005). In order to achieve as complete as possible knowledge of these materials an exhaustive structural, microstructural and magnetic characterization was performed. These samples present effects arising from the variation of size, surface to volume ratio and Zn concentration, which are not easily distinguished from each other. Therefore, their characterization demands the concurrence of complementary experimental techniques such as TEM, XRD, XAS, Mössbauer effect spectroscopy and dc magnetometry. In addition to that, heating efficiency depends on field excitation characteristics f and H_0 and on ferrofluid magnetic and structural properties. Specifically, it depends on MNP composition, size, saturation magnetization and magnetic anisotropy, internal structure and hydrodynamic behaviour. Then, a comprehensive analysis of SAR values becomes a multiparametric problem that requires complete knowledge of the involved materials.

SAR was determined in aqueous suspension as a function of MNP concentration and RF amplitude in a set of twelve suspensions of $Zn_xFe_{3-x}O_4$ nanoparticles. Zn content was varied from $x = 0.0$ to $x = 0.5$, and the nanoparticles were suspended in two biocompatible aqueous liquid carriers of different viscosities. Using the characterization carried out and the linear response theory under the assumption of uniaxial magnetic anisotropy, we were able to merge all SAR data into a single curve. Our results provide insight for the design of more efficient MNPs. They indicate that a further improvement in SAR performance for magnetite-based materials must rely on saturation magnetization enhancement keeping particle size within the order of the resonant size for the working frequency. On the other hand, minor hysteresis cycles were simulated using a two energy level model. This simulation allowed us to establish the influence of anisotropy on retarding SAR saturation effects for increasing field amplitude.

2. Experimental

2.1. Sample preparation

2.1.1. Series 1 (S1) samples. MNPs: Zn-doped magnetite $Zn_xFe_{3-x}O_4$ ($x = 0.0, 0.1, 0.2, 0.3, 0.4, 0.5$) was obtained following a similar procedure employed in Vergés *et al* (2008). $FeSO_4$ precipitation and subsequent ageing were carried out in a closed system consisting of a three-necked round bottom flask placed in a water bath with mechanical stirring. The iron (II) solution was introduced at a constant rate under flowing nitrogen. To prepare the undoped magnetite sample nitrogen was bubbled through two solutions independently: (i) 180 ml of distilled water containing NaOH with a final constant concentration of 7.0×10^{-2} and 0.022 mol l^{-1} KNO_3; and (ii) 20 ml of 7.4×10^{-1} mol l^{-1} $FeSO_4 \cdot 7H_2O$ dissolved in 10^{-2} mol l^{-1} H_2SO_4, heated to 70 °C. After 30 min, the basic solution was added at a constant rate and under mechanical stirring to the iron (II) sulfate solution. Solution temperature and nitrogen bubbling rate were kept constant during the synthesis. When the precipitation was completed, nitrogen was allowed to pass for another 5 min. The system was kept at rest inside a water bath at the same temperature for 2 h. At this point, the solution was cooled down to RT, and the solid was separated by magnetic decantation, washed several times with distilled water and centrifuged. Then, it was dried under vacuum at 40 °C for 24 h. For Zn-doped samples $FeSO_4 \cdot 7H_2O$ was partially replaced by $ZnSO_4 \cdot 7H_2O$, in a fraction corresponding to the desired composition.

FFs: washed S1 particles (10 mg) were dispersed in 3.5 ml of a solution containing 2% chitosan and acetic acid solution (1%w/w) acid, stirred for 6 h at room temperature to ensure that they were coated evenly and subsequently sonicated for 30 min. Coating proceeds through specific interactions between particle surfaces and polymer structural composition.

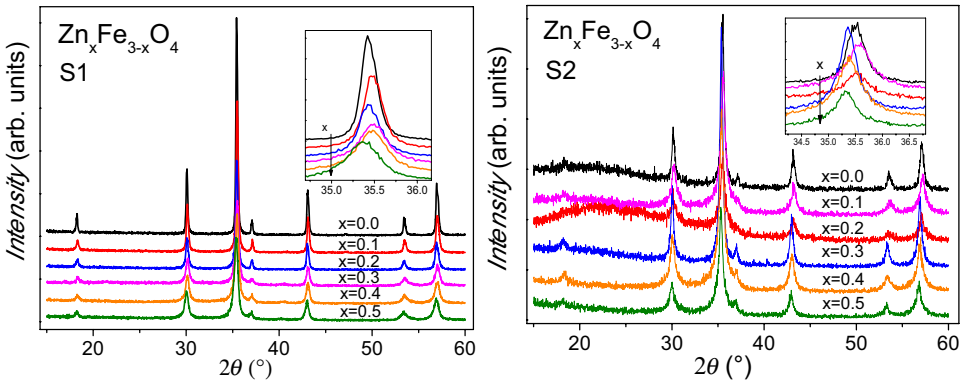

Figure 1. X-ray diffraction patterns of Zn-doped magnetite samples. Insets provide a closer view of the (3 1 1) reflection line. Arrows indicate increasing Zn content.

This FF was purified at RT by centrifugation at 2500 rpm for 10 min and subsequently at 3500 rpm for 15 min, and resuspended in the chitosan solution. The polymer has an amine group that gets positively charged in acetic media; providing colloidal stability. The MNPs remain suspended for several days.

2.1.2. Series 2 (S2) samples. MNPs: were prepared with a procedure similar to that followed for S1 samples. The difference lies in step (i) where 180 ml of distilled water were replaced by 100 ml of absolute ethanol and 80 ml of distilled water.

FFs: washed S2 particles (50 mg) were dispersed in 50 ml of distilled water by sonication for 12 h. In this case, the preparation method promotes surface nanoparticle charge (sulfate ions), to stabilize the nanoparticle dispersion and no surfactant was necessary. The presence of sulfur ions was confirmed by EDAX analysis (not shown).

Hereafter, samples are identified by Zn content x and crystallite size D.

2.2. Sample characterization

XRD was carried out with a X'Pert diffractometer (CuKα radiation with $\lambda = 1.5406$ Å). Data were collected in the $15^\circ \leqslant 2\theta \leqslant 60^\circ$ range, swept at a rate of 5 s per step in 0.02° step scans. Diffractograms were analysed using the MAUD program (Lutterotti 2010), which is based on the Rietveld analysis method.

TEM experiments were carried out using an EM-301 (Philips) microscope, at 100 kV, after a drop of FF was spilled and dried on a carbon-coated copper grid.

Room temperature XANES and EXAFS spectra of the Fe K-edge (7112 eV) and Zn K-edge (9659 eV) were recorded in transmission mode using a Si (1 1 1) monochromator at the XAS beamlines of LNLS (Laboratorio Nacional de Luz Sincrotron) in Campinas, Brazil. The spectral analysis was carried out by pre-edge background subtraction followed by a normalization procedure considering the EXAFS region. The fine structure oscillations $\chi(k)$ of each spectrum in the extended region were isolated using the ATHENA program (Ravel and Newville 2005) and Fourier transformed over a specific k range.

^{57}Fe Mössbauer spectra at 300 K were taken in transmission geometry with a nominal 20 mCi ^{57}Co source in the Rh matrix driven by a triangular velocity wave. Isomer shifts (δ) are referred to metallic α-Fe at RT.

Dc magnetization was recorded versus magnetic field using vibrating sample magnetometers (maximum applied fields $H_{max} = 1190$ and 1430 kA m^{-1}) and a SQUID ($H_{max} = 5570$ kA m^{-1}) magnetometer.

SAR experiments were conducted in a clear glass Dewar containing 1 ml of FF located at the centre of a 5-turn duty coil (25 mm inner diameter). The coil was fed with a 260 kHz ac current. The magnetic field amplitudes H_0 were calculated from the current I through the duty coil. To this end, the H–I correlation was determined using a 4 mm diameter thin sensing coil wound with 20 turns. Field amplitudes of up to 57.7 kA m^{-1} were used in order to study SAR dependence on H_0. Temperature was determined with fibre optic sensors placed in contact with the FF and connected to a calibrated signal conditioner (Neoptix) with an accuracy of ±0.1 K. FF temperature was kept below 45 °C in order to minimize FF evaporation and prevent its destabilization. To study SAR dependence on FF concentration, several dilutions up to 1 : 100 were obtained from samples with initial concentrations c of about 12 kg (MNP)/m^3 (FF). To ensure FF stability, S1 samples were suspended in a chitosan aqueous solution with viscosity $\eta \sim 6 \times 10^{-3}$ Pa s and specific heat $C \sim 4.2 \times 10^3$ J kg^{-1} K^{-1} at RT (η and C measured in the present work). Instead, S2 samples, having smaller size, were suspended in water ($\eta \sim 1 \times 10^{-3}$ Pa s, $C = 4.18 \times 10^3$ J kg^{-1} K^{-1} at RT).

3. Results and discussion

3.1. XRD and TEM characterization

X-ray diffractograms for S1 and S2 samples are shown in figure 1. Only Bragg peaks belonging to the cubic spinel structure appear, indicating that the samples are single phase (JCPDS 19-629).

For each composition the whole spinel pattern (space group $Fd3m$) was refined including peak broadening due to the crystallite size. For S1 samples, as x increases, the mean crystallite diameter D progressively decreases from 117 to

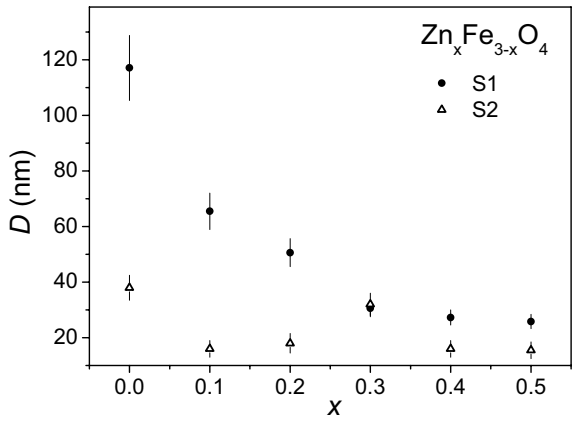

Figure 2. Crystallite size D as a function of Zn concentration for the whole set of samples obtained from the XRD analysis.

26 nm. For S2 samples the x decreasing size tendency is less defined and D ranges between 38 nm for $x = 0.0$ and 15 nm for $x = 0.5$ (see figure 2). The spinel lattice cell parameter was observed to increase from $x = 0.0$ to $x = 0.5$, in about 0.2% (0.5%) for S1 (S2) samples. The shift of the (3 1 1) reflection line to lower angles due to cell expansion is shown in the inset of figure 1. Crystallite sizes and cell parameters are listed in table 1 of the online supplementary data (http://stacks.iop.org/JPhysD/46/125006/mmedia).

Figure 3 displays the TEM images of the samples $x = 0.0$, $D = 117$ nm (S1) and $x = 0.1$, $D = 16$ nm (S2). The images of all the samples showed cubic-like nanoparticles and the observed mean sizes were in good agreement with XRD determinations.

3.2. XAS characterization

The Zn K-edge XANES spectrum reflects the electronic 1s→4p transitions of Zn. The XANES spectrum of normal $ZnFe_2O_4$ is characterized by peaks at energies (see figure 4) about 9664 (peak A), 9668 (peak B) and 9672 eV (peak C), a shoulder at about 9677 eV (peak D), and an additional contribution at higher energies (peak E) (Nakashima *et al* 2007, Stewart *et al* 2007).

As depicted in figure 4, all these features are present in the spectra of both series S1 and S2. In particular, we do not detect any appreciable intensity increment of peak B, which should be noticeable when Zn substitutes Fe at octahedral sites (Nakashima *et al* 2007, Stewart *et al* 2007). We observe that peak B in the spectra of S1 samples $x = 0.1$ and 0.2 is slightly shifted to higher energies (see also the online supplementary data, SD). But as Zn content increases the XANES pattern resembles that of normal $ZnFe_2O_4$. In contrast, S2 samples show the same features for all Zn concentrations. Finally, the prominence of peak D in all S1 and S2 spectra would indicate that Zn electronic transitions mainly involve Zn sites with T_d symmetry (Nakashima *et al* 2007).

The Fe K-edge XANES spectra are shown in figure 5. The pre-edge structure arises from the electronic 1s → 3d quadrupole and 1s → 3d/4p dipole transitions. We observe that the pre-edge intensity for series S1 and S2 is markedly larger than that observed for normal $ZnFe_2O_4$ but lower than the intensity measured for bulk Fe_3O_4 (figures 5(*c*) and (*d*)). This indicates the presence of Fe atoms occupying both non-centrosymmetric A and centrosymmetric B sites in the Zn-doped magnetite sample (Stewart *et al* 2007). The undoped samples present the highest peak intensity compatible with a higher A site occupancy of iron ions. For both series, samples $x = 0.2$, 0.3 and 0.4 show similar pre-edge intensities, while the lower pre-edge contribution of $x = 0.5$ would indicate that more Zn ions occupy A sites replacing Fe ions. On the other hand, the edge-position shift to higher energy is more pronounced for $x = 0.3$, 0.4 and 0.5 (S1 series). This is compatible with a tendency towards +3 iron oxidation state as Zn progressively replaces Fe^{2+} at A sites. Features above the edge resemble those of Fe_3O_4 compound (figure 5). No other remarkable observations are appreciable that can be correlated with the Zn content, which is expected due to low Zn : Fe ratio.

The detailed analysis carried out on the EXAFS region at Fe and Zn K-edges is included in the online supplementary data. From these studies we observe the following: (i) the Fourier transforms (FT) of $\chi(k)$ at Zn K-edge show a reduction in the main peak amplitude when compared with bulk $ZnFe_2O_4$, probably due to surface disorder, (ii) fitting considering the first coordination shell gave a coordination number N near four for the Zn central atom (see the online supplementary data), while N of the Fe central atom approximates six when doping increases; (iii) the shoulder in the Zn FT of the peak centred at 3.1 Å that usually appears when Zn occupies B sites (Ammar *et al* 2004, Stewart *et al* 2007) is absent in all the samples (see the online supplentary data).

3.3. Mössbauer effect spectroscopy results

RT Mössbauer spectra are shown in figure 6. In both series a gradual change from bulk like to magnetically relaxed and/or compositionally disordered states is observed as x increases. Indeed, absorption lines broaden while spectral central contribution grows as Zn content increases.

The $x = 0.0$ spectra display two well resolved magnetic subspectra, especially for the $D = 117$ nm sample (S1), with magnetic hyperfine fields (B_{hf}) of 49.0 ± 0.1 and 46.0 ± 0.1 T, δ of 0.26 ± 0.01 and 0.63 ± 0.01 mm s^{-1}, and nearly null quadruple shift (ε). These parameters are in good agreement with those reported for bulk Fe_3O_4 (Vandenberghe *et al* 2000). The narrower sextet with the larger B_{hf} and the smaller δ is associated with high spin Fe^{3+} ions occupying A sites, while the other one is assigned to Fe^{3+}/Fe^{2+} ions occupying B sites. We observe that B_{hf} distribution at B sites broadens as a consequence of the gradual incorporation of Zn^{2+} at A sites and the development of different metal ion configurations around B sites.

These spectra were fitted by assuming Voigtian line shapes (Lorentizian lines of constant width $\Gamma = 0.21$ mm s^{-1} and Gaussian distributions of variable dispersion σ). A consistent fit of the whole set of spectra was achieved considering one magnetic interaction associated with the A site, two

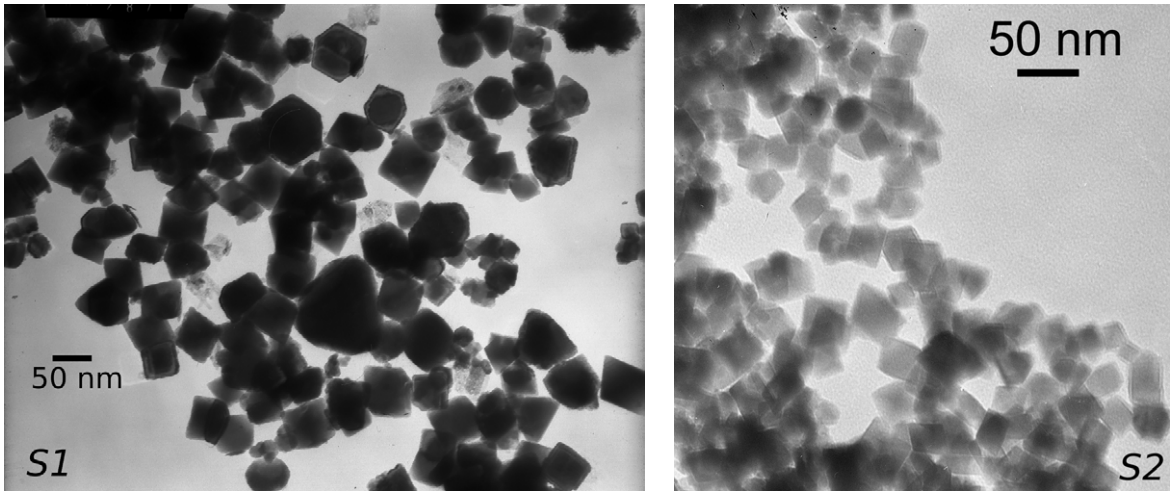

Figure 3. TEM micrographs of samples $x = 0.0$, $D = 117$ nm (S1) and $x = 0.1$, $D = 16$ nm (S2).

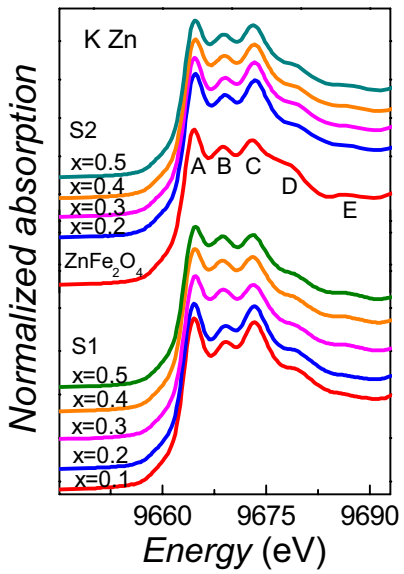

Figure 4. Zn K-edge XANES spectra.

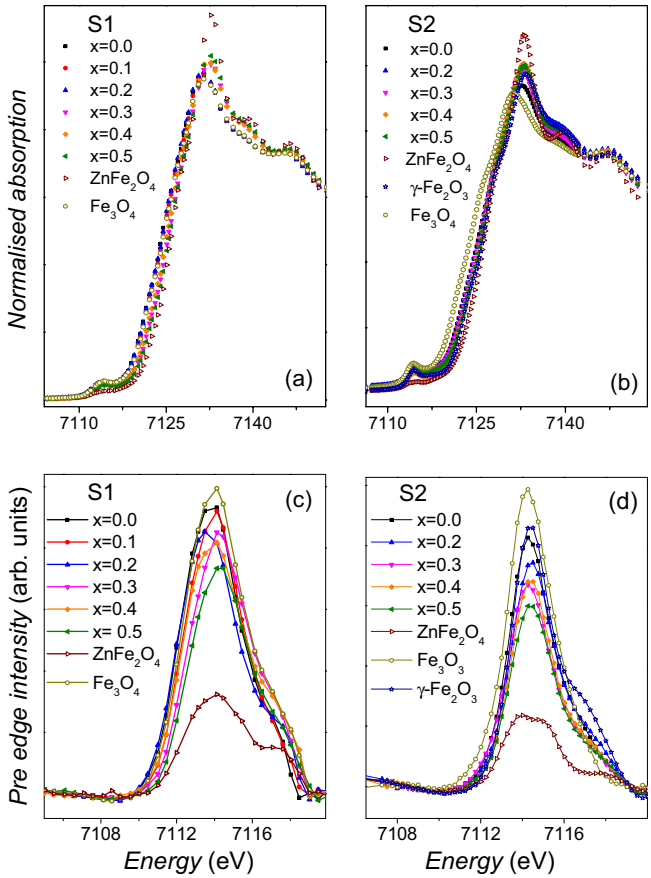

Figure 5. Fe K-edge XANES spectra of S1 (*a*) and S2 (*b*) series. The pre-edge region after discounting the edge jump contribution of S1 (*c*) and S2 (*d*). Spectra of Fe_3O_4, $ZnFe_2O_4$ and γ-Fe_2O_3 bulk compounds are also included for comparison.

magnetic interactions associated with the B site with different distribution widths but restricted to have equal hyperfine parameter correlations, a partially resolved sextet associated with Fe probes experiencing relaxation times $\tau \sim 1/f_L$ (slow-relaxing component), and a doublet related to probes with $\tau < 1/f_L$ (fast-relaxing component), f_L being the Larmor frequency.

The influence of particle size and Zn concentration on the spectral shape can be distinguished considering the following arguments: (i) particle size diminution leads to increasing relaxation effects due to the reduction in magnetic anisotropy energy barrier between MNP magnetic moment opposite direction states; (ii) Zn addition increases relaxation effects via A–B exchange coupling weakening. This also induces line broadening due to the increase in chemical disorder, especially around Fe ions at B sites.

Due to the size effect S1 spectra are, for all compositions, better resolved than S2 ones. For S2 spectra, relaxation effects are larger for $x = 0.2$, $D = 18$ nm than for $x = 0.3$, $D = 32$ nm, indicating that the size effects are stronger than Zn concentration effects. A common feature emerging from both series is that relaxation effects involve a large fraction of probes for D of about 32 nm or smaller. The size at which the well resolved and the fast-relaxing components contribute with similar areas defines the mean crystallite blocking size D_B, which is about 13–15 nm at RT (see figures 6 and 7).

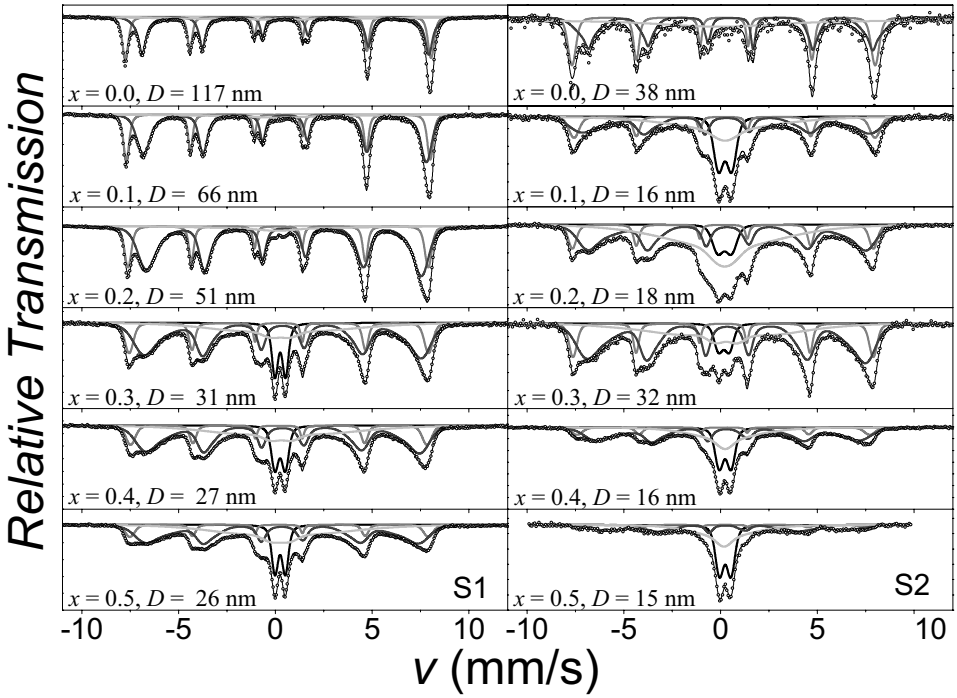

Figure 6. RT Mössbauer spectra of S1 and S2 Zn-doped magnetite MNPs. Experimental data (dots), fitted results (black line) and subspectra components: spinel B site (thin dark grey), spinel A site (medium grey), slow-relaxing (light grey) and fast-relaxing (thick black). Each sample is identified by Zn content x and mean crystallite size D.

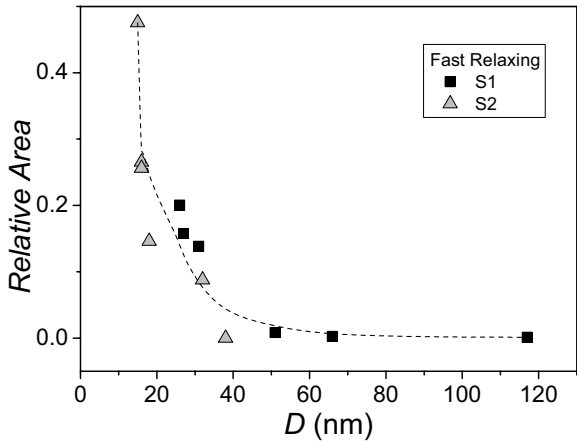

Figure 7. Normalized Mössbauer relative area of the contribution coming from fast-relaxing sites as a function of crystallite size for S1 and S2 samples. Normalization was carried out with respect to the sum of fast-relaxing and non-relaxing components areas. The dashed line is a guide to the eye.

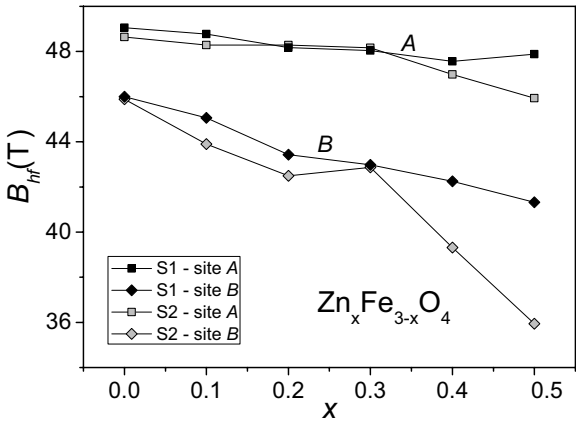

Figure 8. Mean $B_{\rm hf}$ values of the A and B site contributions as a function of x for S1 and S2 samples.

To perform this estimation, we have considered that the slow-relaxing component corresponds to particles whose sizes are about the blocking size $D_{\rm B}$.

The Mössbauer effect time window is given by $1/f_{\rm L}$. We consider a Néel relaxation mechanism, characterized with a relaxation time $\tau_{\rm N} = \tau_0 \exp(KV/kT)$, where τ_0 is the attempts time, K is the anisotropy energy density, V is the particle volume and k is the Boltzmann constant. Using $\tau_0 \sim 10^{-9}$ s (Hergt *et al* 2006, Fortin *et al* 2008) and $K = 1.89 \times 10^4$ J m^{-3} (Fiorani *et al* 2002), the magnetic-core mean blocking size of our magnetite MNPs was estimated as $D_C = [(kT/K)\ln(1/f_{\rm L}\tau_0)]^{1/3} \approx 9.5$ nm. We have estimated $f_{\rm L} \sim 0.3 \times 10^8$ s^{-1} for ^{57}Fe in bulk magnetite from its $B_{\rm hf}$ energy splitting. Assuming a surface 'dead layer' of thickness $t \sim 2.0$–2.5 nm (Kaiser and Miskolczy 1970, Kim *et al* 2001, Knobel *et al* 2008), a size $D \sim D_{\rm c} + t \sim 13.5$–$14.5$ nm is obtained in good agreement with our previous estimation from the Mössbauer blocking temperature. This agreement gives support to the numerical values chosen for τ_0 and K that will be used for SAR data analysis.

When x increases and/or D decreases we observe that (i) the relative area of the well resolved component originated in A site Fe probes decreases. (ii) $B_{\rm hf}$ decreases faster at the B site than at the A site (see figure 8). (iii) As D decreases from 38 nm downwards the fast-relaxing component area increases

steadily (see figure 7). For $D \geqslant 38$ nm the relative value of the two relaxing components area amounts to a total of 10–15% and corresponds almost exclusively to the slow-relaxing contribution. (iv) Hyperfine parameters associated with the B site are strongly affected by Zn addition and their absorption lines broaden considerably with x (see figure 6).

For samples with $x \geqslant 0.3$ or $D \leqslant 32$ nm the relaxation effects are dominant. Further, the slow-relaxing component increases dramatically, while the central doublet appears and grows (fast-relaxing component, figure 6). The central doublet parameters are quadrupole splitting $\Delta = 0.54\,\mathrm{mm\,s^{-1}}$, $\delta = 0.35\,\mathrm{mm\,s^{-1}}$ and $\sigma = 0.24\,\mathrm{mm\,s^{-1}}$. The B_{hf} of the A and B sites decrease with x, this reduction being much more pronounced for the site B (figure 8). The coexistence of magnetically split contributions along with a doublet indicates the simultaneous presence of blocked and unblocked MNP moments. This analysis in terms of blocked and unblocked MNP moments is consistent with the theoretical estimation of the maximum linear dimensions of single-domain magnetite particles of about 130 nm (Sorensen 2001).

When doping magnetite with zinc at the A site the ion distribution can be depicted as $(Zn_x^{2+}Fe_{1-x}^{3+})_A[Fe_{1-x}^{2+}Fe_{1+x}^{3+}]_B O_4^{-2}$. As each Fe^{3+} or Fe^{2+} at the B site has six nearest-neighbour metal ions at A sites, the B site Mössbauer lineshape can be considered as a superposition of components arising from different nearest neighbour A site configurations (Vandenberghe and de Grave 1989). The addition of each Zn^{2+} ion at an A site breaks four Fe(A)-O-Fe[B] super-exchange paths. For each broken A–B path $B_{\mathrm{hf}}^{\mathrm{B}}$ should decrease resulting in a broadening of B sites spectral contribution. In contrast, the effect of broken paths on $B_{\mathrm{hf}}^{\mathrm{A}}$ is expected to be much smaller due to the lower contribution from supertransferred B_{hf} (Vandenberghe and de Grave 1989). Therefore, the reduction in B_{hf}^{B} mean value, the broadening of its distribution and the decrease in the relative area of the A site signal with doping can be related to the inclusion of Zn^{2+} at the A site replacing Fe^{3+} ions. In order to maintain charge neutrality some oxygen vacancies must be generated or a fraction of Fe^{2+} must be transformed into Fe^{3+}, as proposed by Wen *et al* (2006). In figure 9 we observe that while δ_A remains almost unaltered when doping with zinc, the average δ_B decreases monotonically from 0.52 to 0.35 mm s^{-1}. This behaviour is consistent with an increase in the fraction of iron ions at B sites that change their valence from +2 to +3. The δ values corresponding to the slow-relaxing contribution are similar to those of iron at the B site for the whole concentration range, whereas the fast-relaxing component presents δ values intermediate between δ_{A} and δ_{B} ones. The δ behaviour displayed in figure 9 indicates that the slow- and fast-relaxing components correspond to iron probes at B, and at the A and B sites, respectively. Using the δ values we have estimated the relative fraction of Fe in the B and A sites. These results are shown in figure 10. For $x = 0.0$ the area ratio B/A is close to 2, the value ideally expected for the Fe_3O_4 structure. The relative fractions of Fe ions at the A and B sites calculated assuming that Zn exclusively enters into the A site are represented by dashed lines in figure 10, which follow the experimental data closely. The relaxing contributions originate in the superparamagnetic behaviour of the smallest particles whose fraction

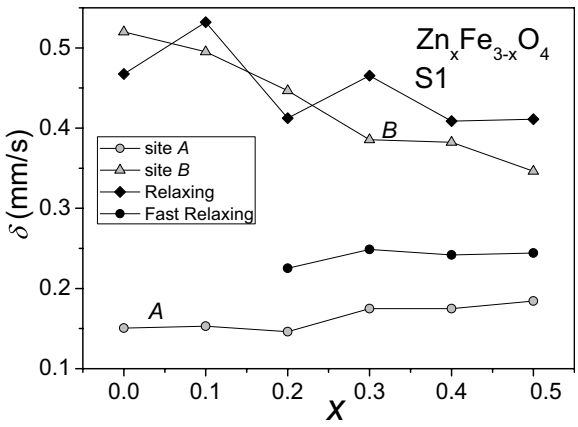

Figure 9. Component isomer shift δ values as a function of x for S1 series.

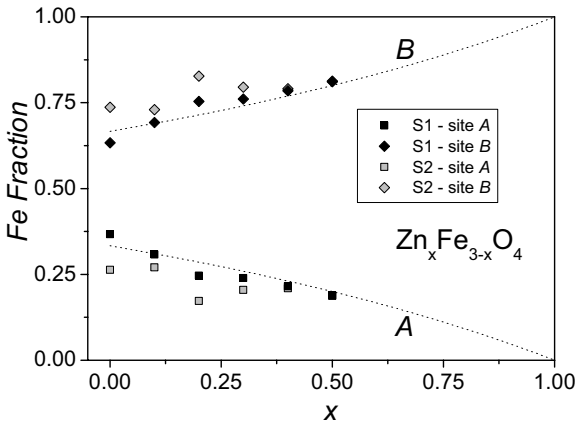

Figure 10. Fe fractions in spinel A and B sites against x for the sample sets S1 and S2 derived from Mössbauer analysis. The dashed lines stand for fractions calculated assuming that Zn enters only at spinel A site.

presents an overall growing trend with decreasing x. As stated before, the relaxation may also originate from A–B super exchange path interruptions due to the presence of non-magnetic Zn^{2+} ions at A sites. This scenario along with the random distribution of Zn^{2+} would bring about magnetic clusters that also undergo spin relaxation and superparamagnetism.

3.4. Dc magnetic studies

The field dependence of the magnetization recorded at 300 K is shown in figure 11. We observe that adding Zn^{2+} ions modifies the MNP ferrimagnetic response producing maximum saturation values of M_s[4] at $x = 0.1$ for S1 and at $x = 0.3$ for S2. $M_s(x)$ decreases steadily for $x > 0.3$, reaching its minimum value at $x = 0.5$ for both series. Similar behaviour is found for the coercive field (H_C) as a function of x (figure 12(b)). The M_s increase with respect to undoped samples ($x = 0.0$) can be interpreted in terms of elimination of Fe^{3+} moment cancellation at neighbouring A and B sites,

[4] For simplicity we use M_s to refer to the value of M obtained for the maximum applied fields during the M versus H experiments, although saturation is not fully achieved at those fields.

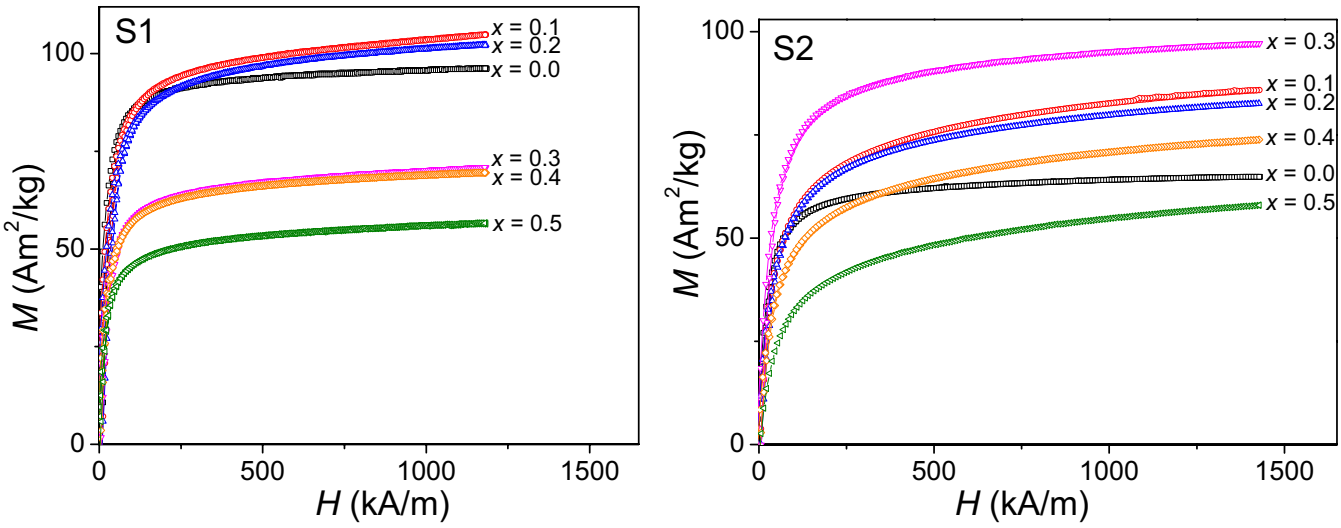

Figure 11. Magnetization M versus applied field H at 300 K for sets S1 and S2. For clarity only the first quadrant is shown.

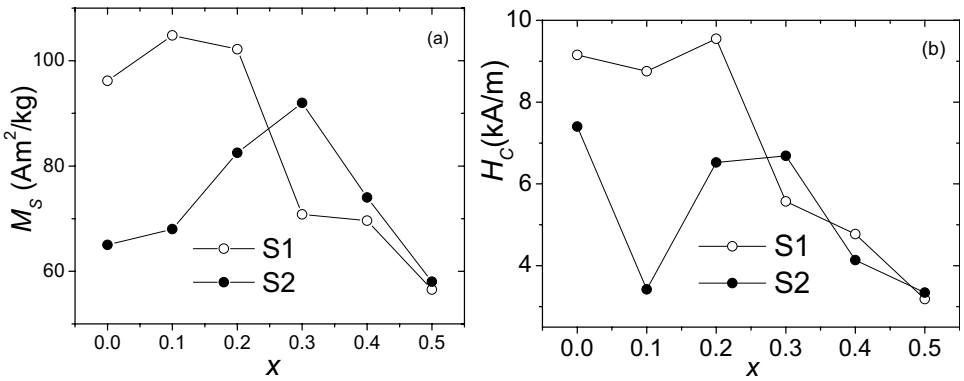

Figure 12. (*a*) Room temperature magnetization M_s at 1200 kA m^{-1} for S1 and S2 sets, as a function of x. (*b*) Coercive field H_C for sets S1 and S2, as a function of x.

since Zn^{2+} incorporation at A sites locally switches off A–B superexchange. Therefore a net moment of $10\mu_B$ per unit formula appears where Zn^{2+} was incorporated, instead of the $4\mu_B$ of undoped magnetite.

The reduction in $M_s(x)$ for $x \geqslant 0.3$ is mostly a compositional effect related to changes in Fe population at the A and B sites, which modify the resulting average moment. Further weakening of the A–B interaction and the consequent takeover of the B–B one when Zn^{2+} A site occupation is sufficiently high, lead to a reduced moment per unit formula.

For both series, the $M_s(x)$ behaviour resembles the D dependence with x (figure 2). It is expected that the size effect might have secondary influence on the observed M_s drop for $x \geqslant 0.3$, since crystallite size changes are less pronounced for this composition range (see figure 2).

3.5. SAR and related studies

Magnetic hyperthermia relies on the ability of MNPs to absorb power from a RF field. This property is expressed by the SAR, which is the power absorbed per unit mass of MNPs[5]. SAR depends on RF field amplitude and frequency, and on the MNP properties reported in the previous section. Other MNP properties like magnetic anisotropy, internal structure and hydrodynamic behaviour strongly affect the magnetic moment relaxation time τ. In order to get more insight into their effect on SAR, inversion field (H_i) versus maximum applied field H_{max} (up to 1.43×10^6 A m^{-1}) were measured at RT. Furthermore, estimations of SAR were carried out using a two-level model for the MNP spin orientation state, and a comprehensive analysis of SAR experimental results is addressed.

Temperature T versus time t curves were recorded for all the samples for $H_0 \leqslant 57.7$ kA m^{-1} (see the insets of figures 13(*a*) and (*b*)). Figure 13(*a*) shows $\Delta T/\Delta t$ slopes of the initial linear region of $T(t)$ curves recorded from the $x = 0.2$, $D = 18$ nm (S2) sample as a function of H_0^2. This initial linear response was observed for all the samples, indicating that our experimental device behaves almost adiabatically during short periods of time ($t \leqslant 20$ s) for ΔT of at least 20 K. The experimental SAR values were retrieved from the measured slopes using the expression (Vergés *et al* 2008)

$$\mathrm{SAR} = \frac{C}{\phi}\Delta T/\Delta t, \quad \phi = \frac{m_{\mathrm{MNP}}}{m_{\mathrm{FF}}}, \tag{1}$$

[5] For consistency with most reported data SAR values are given in W g^{-1}.

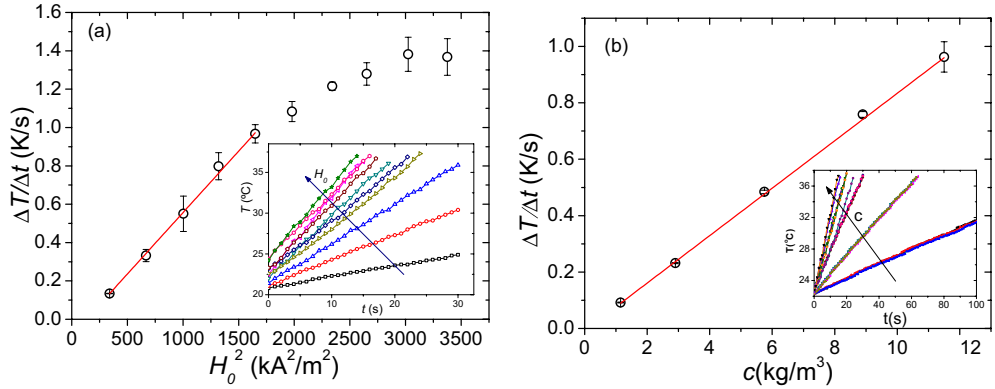

Figure 13. (*a*) Initial slopes $\Delta T/\Delta t$ for sample $x = 0.2$, $D = 18$ nm (S2) as a function of square field amplitudes H_0^2 showing a saturation effect for $H_0 > 41\,\mathrm{kA\,m^{-1}}$. (*b*) $\Delta T/\Delta t$ dependence on FF concentration c for sample $x = 0.1$, $D = 16$ nm (S2). Insets: initial linear region of $T(t)$ curves for $18\,\mathrm{kA\,m^{-1}} \leqslant H_0 \leqslant 57.7\,\mathrm{kA\,m^{-1}}$ (*a*); and $1\,\mathrm{kg\,m^{-3}} \leqslant c \leqslant 12\,\mathrm{kg\,m^{-3}}$ (*b*).

where C is the FF specific heat and m_{FF} and m_{MNP} are the masses of FF and MNPs in the Dewar, respectively. A linear dependence on ferrofluid concentration $c = \phi\rho_{\mathrm{FF}}$ (ρ_{FF} is the FF mass density) was observed for the whole concentration range, as shown in figure 13(*b*) for $x = 0.1$, $D = 16$ nm (S2). This result rules out effects of MNP interactions or aggregation during RF irradiation on the measured SAR. SAR versus H_0 behaviour was investigated in the range $18\,\mathrm{kA\,m^{-1}} \leqslant H_0 \leqslant 57.7\,\mathrm{kA\,m^{-1}}$. The quadratic H_0 dependence expected from the linear response theory (Rosensweig 2002)

$$\mathrm{SAR} \approx \frac{\pi\mu_0 H_0^2 f}{\rho}\chi''; \quad \chi'' = \frac{\mu_0 M_S^2 V\rho^2}{3kT}\frac{\omega\tau}{1+(\omega\tau)^2} \tag{2}$$

was found to hold up to $H_0 \sim 41\,\mathrm{kA\,m^{-1}}$ for all the samples, as shown in figure 13(*a*) for $x = 0.2$, $D = 18$ nm (S2). In equation (2) χ'' is the susceptibility dissipative component, ρ is the MNP density, V its volume, τ its magnetic moment relaxation time and $\omega = 2\pi f$ is the excitation angular frequency. A tendency to saturation is observed for higher H_0 values. This effect originates from the saturation of the M versus H cycle area,

$$\mathrm{SAR} = f\varepsilon_{\mathrm{cycle}} = -f\mu_0 \oint_f M\,\mathrm{d}H, \tag{3}$$

where $\varepsilon_{\mathrm{cycle}}$ is the energy per mass unit dissipated in one cycle and $\oint_f$ indicates that the cycle is performed at the frequency f.

Due to the lack of appropriate analytical expressions for evaluation of equation (3) we have estimated SAR dependence on H_0 using a two energy level model for the MNP magnetic moment orientation state (Carrey *et al* 2011). This estimation was performed for the $x = 0.2$, $D = 18$ nm sample (S2). This model assumes uniaxial anisotropy and considers thermal activated transitions of the magnetic moment over the anisotropy energy barrier. Moment oscillations around each of the two energy minima were disregarded. The assumption of Néel relaxation will be justified below, where we will conclude that this mechanism dominates for sizes $D \leqslant 18$ nm. When a field is applied parallel to the anisotropy axis the Zeeman and anisotropy interactions can be described as

$$E = KV\sin^2\theta - \mu_0 V M_s H\cos\theta, \tag{4}$$

where θ is the angle between the magnetic moment and the field. For $|H| < H_K \approx 2K/\mu_0 M_s$ the energy barriers seen by moments oriented at angles $\theta = 0$ and $\theta = \pi$ have heights $E_\pm = KV(1\pm h)^2$; where $h = H/H_K$. The frequency for the transition from $\theta = \pi$ to $\theta = 0$ is given by $\nu_1 = \nu_0 \mathrm{e}^{-E_-/kT}$ and by $\nu_2 = \nu_0 \mathrm{e}^{-E_+/kT}$ for the opposite one. Calling P_1 the state 1 occupation probability, gives the following differential equation

$$\frac{\mathrm{d}P_1}{\mathrm{d}t} = \nu_1 - \frac{(\nu_1+\nu_2)}{2}P_1. \tag{5}$$

Taking into account that $\mathrm{d}/\mathrm{d}t = (\mathrm{d}/\mathrm{d}H)(\mathrm{d}H/\mathrm{d}t)$ and that $M = M_s(2P_1 - 1)$, equation (5) becomes

$$\frac{\mathrm{d}M}{\mathrm{d}H} = \frac{2M_s\left\{\nu_1 - \left(\frac{\nu_1+\nu_2}{2}\right)\left(\frac{M}{M_s}+1\right)\right\}}{\mathrm{d}H/\mathrm{d}t}. \tag{6}$$

Assuming for simplicity that the field is a periodic triangular function of time, $\mathrm{d}H/\mathrm{d}t$ takes alternating constant values $\pm 4fH_0$, and equation (6) can be solved by numerical methods. From here, SAR can be evaluated using (3), whatever f and H_0 are. The assumption that the anisotropy axis is parallel to the applied field is reasonable for the Néel relaxation mechanism and not too high frequency. Under these conditions the energy minimum occurs for parallel orientation, leading to an effective orientation of the MNP easy axes along the field. M versus H cycles simulated for $f = 260\,\mathrm{kHz}$, $\nu_0 = 10^9\,\mathrm{s^{-1}}$, $K = 1.89\times10^4\,\mathrm{J\,m^{-3}}$, $V = 5.832\times10^{-24}\,\mathrm{m^3}$ (cubic MNP) and $T = 310\,\mathrm{K}$, for increasing values of H_0 are shown in figure 14(*a*). A maximum inversion field $H_i^{\mathrm{RF}} \approx 20.7\,\mathrm{kA\,m^{-1}}$ is observed. The dependence of SAR on H_0, calculated for the stated values of $K = 1.89\times10^4$ and $2.47\times10^4\,\mathrm{J\,m^{-3}}$, is presented in figures 14(*b*) and (*c*), respectively. The fact that the experimental SAR values obtained for $H_0 = 41\,\mathrm{kA\,m^{-1}}$ (see figure 17(*b*)) are at least six times smaller than those shown in figure 14 could be attributed to the broad particle size distribution ($\sigma_D \sim 10$ nm, see below). On the other hand, a quasilinear dependence on H_0^2 is found for $H_0 < 25.1\,\mathrm{kA\,m^{-1}}$ (figure 14(*b*)) and $H_0 < 39.8\,\mathrm{kA\,m^{-1}}$ (figure 14(*c*)), in agreement with the experimental results shown in figure 13(*a*). The dependence on K of the field value at which the curve

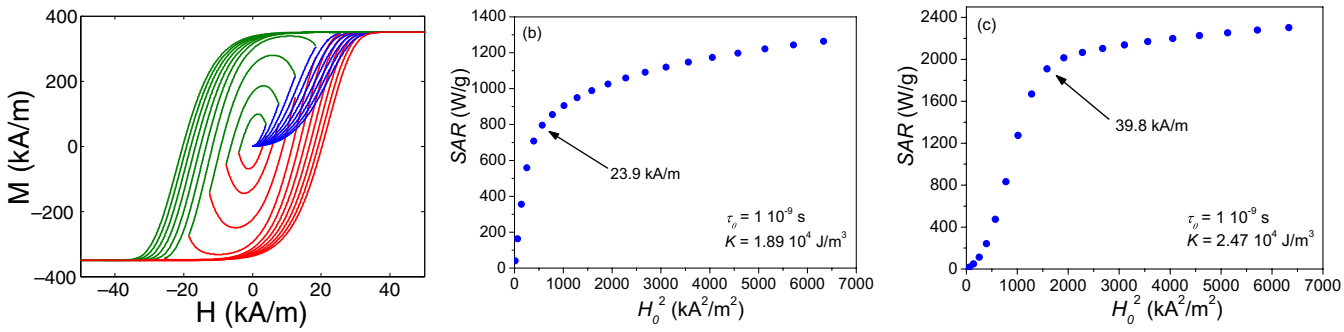

Figure 14. (*a*) M versus H loops calculated for $x = 0.2$, $D = 18$ nm sample (S2) and several H_0 values using the two-level approach for MNP Néel moment relaxation. (*b*) and (*c*) show SAR versus H_0^2 for two anisotropy constant K values.

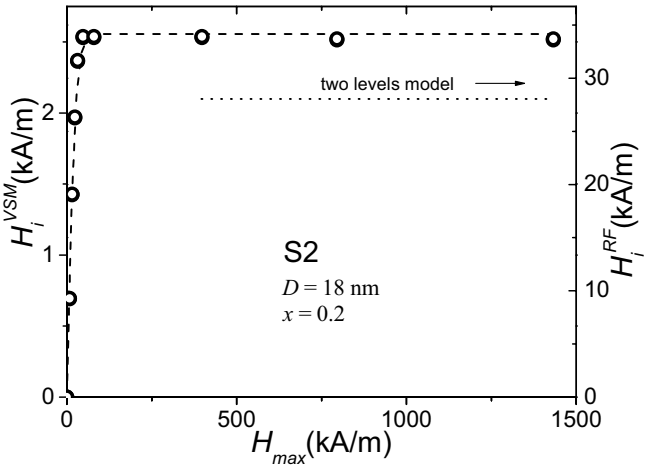

Figure 15. Inversion field. Left scale stands for H_i^{VSM} retrieved from RT VSM minor loops of $x = 0.2$, $D = 18$ nm sample (S2) recorded using several $H_{\max}$ values. Right scale stands for H_i^{RF} values calculated with equation (7). The dashed line is a guide to the eye. The dotted line indicates the maximum H_i^{RF} value obtained with the two-level model.

slope suddenly diminishes, reveals the influence of anisotropy on retarding SAR saturation effects.

Next, to experimentally test the model, the inversion field (H_i^{VSM}) was measured using a VSM and subsequently scaled to RF frequency. H_i^{VSM} values retrieved from minor M versus H cycles registered for the $x = 0.2$, $D = 18$ nm sample are shown in figure 15. The scaling was carried out assuming that the expression $H_{\mathrm{C}}(T) = H_{\mathrm{C}}(0)\{1 - \sqrt{\alpha \ln(\tau_{\mathrm{obs}}/\tau_0)}\}$ (Cullity and Graham 2009) is also valid for H_{i},

$$H_{\mathrm{i}}^{\mathrm{RF}}(H_0) = \frac{1 - \sqrt{-\alpha \ln(f\tau_0)}}{1 - \sqrt{-\alpha \ln(f_{\mathrm{VSM}}\tau_0)}} H_{\mathrm{i}}^{\mathrm{VSM}}(H_0), \qquad (7)$$

where $\tau_0 = \nu_0^{-1} = 10^{-9}$ s, $\alpha = kT/KV$ and the 'frequency' f_{VSM} was estimated from VSM recording time τ_{VSM} as $f_{\mathrm{VSM}} \approx \tau_{\mathrm{VSM}}^{-1}(\tau_{\mathrm{VSM}} \sim 30\,\mathrm{s})$. The conversion factor from VSM to RF was ~13.4. We have found that the $H_{\mathrm{i}}^{\mathrm{RF}}$ values obtained with the two-level model are 61% of those retrieved from $H_{\mathrm{i}}^{\mathrm{VSM}}$ and equation (7) as indicated in figure 15. The $H_{\mathrm{i}}^{\mathrm{RF}}$ values obtained from the two-level model were in acceptable agreement with those estimated by frequency scaling $H_{\mathrm{i}}^{\mathrm{VSM}}$.

The SAR values obtained from S1 MNPs in the chitosan suspension for H_0 values between 18 and 57.7 kA m^{-1} are shown in figure 16(*a*). The behaviour is regular and dominated by size. The highest SAR occurs for $x = 0.0$, $D = 117$ nm, 323 W g^{-1} being the maximum registered value at $H_0 = 41$ kA m^{-1}. The intrinsic loss power values ILP = SAR/($H_0^2 f$) are close to 0.5 nH m^2 kg^{-1}. These ILP values are four to five times lower than recently reported results (Behdadfar *et al* 2012), probably due to the quite large size dispersion observed in our samples.

The SAR values obtained from aqueous S2 suspension, for $H_0 = 41$ kA m^{-1}, seem to present more erratic behaviour with x (figure 16(*b*)). They show a pronounced maximum value of 367 W g^{-1} for $x = 0.1$, $D = 16$ nm.

To reveal the influence of the frequency factor $\omega\tau/(1 + (\omega\tau)^2)$ of the susceptibility dissipative component (equation (2)), we have normalized the whole set of SAR values by $M_{\mathrm{s}}^2 V H_0^2$. To adjust these normalized data to the frequency factor expression the set was constrained to a maximum value of 0.5. The result, shown in figure 17, displays consistent behaviour for the whole set of samples. These data were analysed assuming the possibility of Néel and Brown relaxation processes. For the first one, $K = 1.89 \times 10^4$ J m^{-3}, $\tau_0 = 10^{-9}$ s and a dead magnetic layer of thickness t were considered, consistent with Mössbauer data analysis. The MNP size was set as $D = D_C + 2t$, with $t \approx 2$ nm. For the second relaxation mechanism ($\tau_{\mathrm{B}} = 3\eta V_{\mathrm{h}}/kT$), values of η between 1×10^{-3} and 6×10^{-3} Pa s were used. The effective relaxation time was calculated from $\tau = ((1/\tau_{\mathrm{N}}) + (1/\tau_{\mathrm{B}}))^{-1}$. Reasonable agreement was found between experimental data and simulations represented in figure 17. The best description was achieved for $\eta \sim 2 \times 10^{-3}$ Pa s. This is an acceptable value considering that most results come from chitosan MNP suspensions (S1). Indeed, chitosan solution has a viscosity of 6×10^{-3} Pa s at 293 K, but it is well known that liquid viscosity drops rapidly with temperature, thus making this result plausible. Most S2 samples, suspended in water, have sizes below the crossover from the Néel to Brown mechanism (~18 nm, figure 18). Then, they do not influence the overall behaviour of normalized SAR values at the Brown relaxation region. The maximum frequency factor is achieved for $D \sim 16$ nm (figure 17). However, the best SAR values corresponded, in order of performance, to $x = 0.1$, $D = 18$ nm; $x = 0.0$, $D = 117$ nm and $x = 0.3$, $D = 32$ nm. This difference is due to the influence of the $M_{\mathrm{s}}^2 V$ factor on SAR. In this work, due to the wide range of grain sizes, the volume dominates the behaviour of S1 samples.

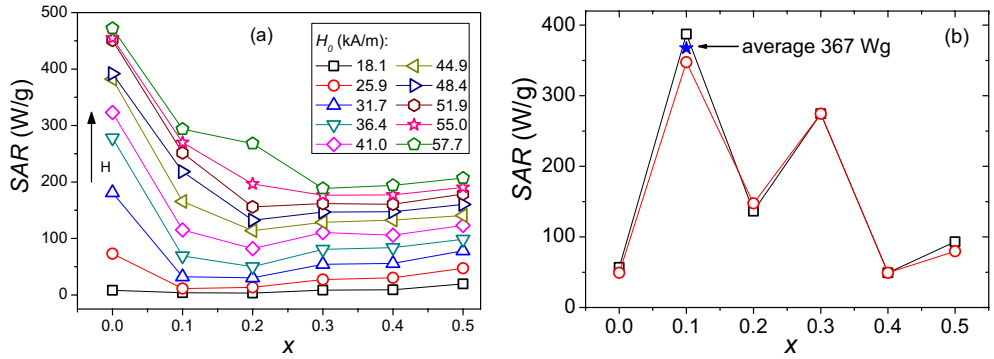

Figure 16. (*a*) S1 series SAR values as a function of x, for H_0 values indicated at the upper right. (*b*) The same for S2 series obtained from both SAR versus FF composition (circles) and from SAR versus H_0 measurements (squares) for $H_0 = 41\,\mathrm{kA\,m^{-1}}$.

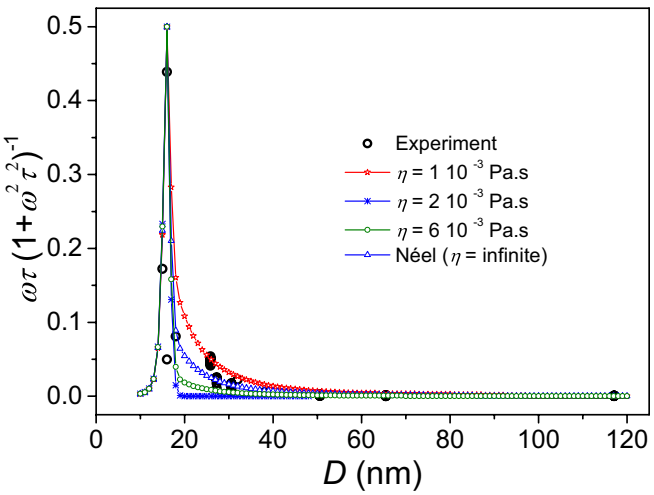

Figure 17. Dependence of the frequency factor $\omega\tau/1 + (\omega\tau)^2$ of the dissipative susceptibility component on the MNP mean size for the whole set of samples.

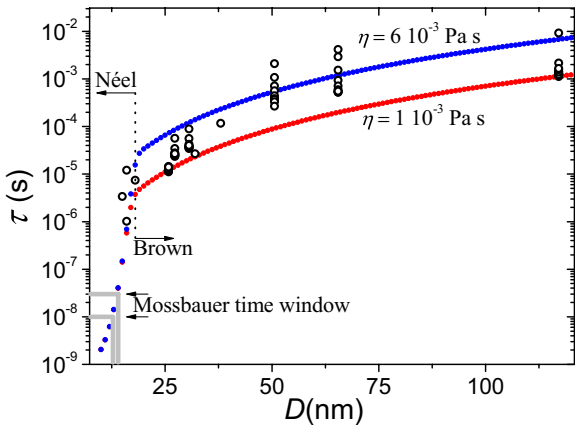

Figure 18. Experimental relaxation times τ obtained from $\omega\tau/1 + (\omega\tau)^2$ (figure 17): open dots. Filled dots stand for the values calculated considering the Néel and Brown relaxation mechanisms, for two different viscosity values.

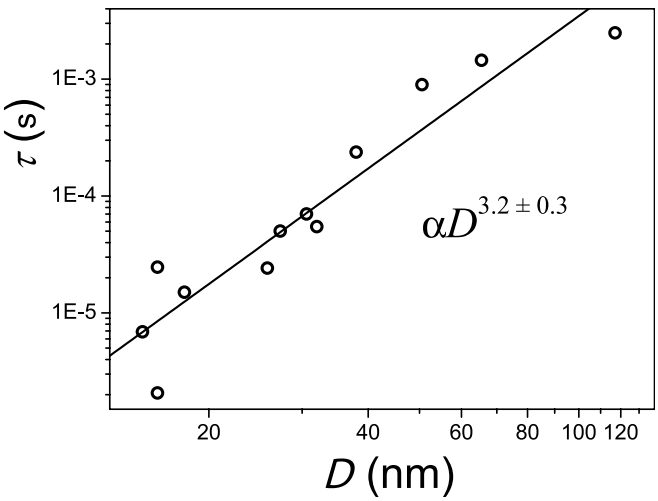

Figure 19. Log–log plot of experimental relaxation times versus crystallite size D. Only the subset obtained using $H_0 = 41\,\mathrm{kA\,m^{-1}}$ is shown. The solid line is the result of a linear fit as described in the text.

However, the volume increase of almost 400 times from 15 to 117 nm samples is approximately compensated by the sharp frequency factor decrease. To take advantage of the volume factor in equation (2), frequency should be shifted to a lower value, i.e. to one which makes 117 nm the resonant size. But this would have a drawback since SAR increases monotonically with frequency. Therefore, frequencies in the range 0.1–1 MHz should be used in order to attain efficient SAR performance.

The RT relaxation time τ dependence on D was calculated with the stated values of τ_0, K and t, for the two extreme η values: 1×10^{-3} and 6×10^{-3} Pa s (see figure 18). The Mössbauer observation time window is also indicated in the figure. The experimental τ values retrieved from figure 17 are in good agreement with those calculated using the chosen Néel and Brown relaxation mechanism parameters (see figure 18). Figure 19 shows the subset of experimental values retrieved using $H_0 = 41\,\mathrm{kA\,m^{-1}}$ plotted in a log–log scale. A linear fit performed on these data gives a slope of 3.2 ± 0.3, which confirms the Brown relaxation process dominance for $D \geqslant 18$ nm ($\log \tau_B \propto 3D$).

4. Conclusions

A detailed study of $Zn_xFe_{3-x}O_4$ cubic-like MNPs was carried out in order to achieve a complete characterization

of the physical properties which influence power absorption performance from a radio-frequency field within the framework of the linear response theory. A wide range of compositions and sizes ($0.0 \leqslant x \leqslant 0.5$, $15\,\text{nm} \leqslant D \leqslant 117\,\text{nm}$) was investigated. It was demonstrated that Zn^{2+} ions enter selectively into spinel A sites. Consistently, M_s presents maximum values for $x = 0.1$–0.3 owing to the influence of Zn on superexchange interaction paths. From the observation of MNP magnetic moments relaxation with the Mössbauer effect time window, plausible values of $\tau_0 = 1 \times 10^{-9}$ s and $K = 1.89 \times 10^4\,\text{J m}^{-3}$ were selected. These values were adopted for subsequent simulations and analyses.

The SAR dependence on x and D could be interpreted with the linear response theory for field amplitudes $H_0 \leqslant 41\,\text{kA m}^{-1}$. At $H_0 = 41\,\text{kA m}^{-1}$ the maximum value of 367 W per gram of MNP was obtained for the $x = 0.1$, $D = 16\,\text{nm}$ sample. SAR saturation was observed at higher fields. It was explained by means of simulations performed within the two-level approximation for the Néel magnetic moment relaxation. These simulations indicated that increasing MNP effective anisotropy improves magnetic hyperthermia performance at higher fields. This improvement comes from the shift of the H_0 limit for the quasilinear SAR versus H_0^2 dependence towards higher field values. Low-frequency inversion fields of minor cycles were measured. Using a scaling procedure valid for coercive fields, inversion field values consistent with those calculated for RF frequency with the two-level model were obtained, suggesting that this scaling may be useful for SAR data analysis.

Using the information obtained through the exhaustive MNP characterization carried out in this work, a self-consistent description of the whole set of sample behaviour was attained. The frequency factor $\omega\tau(1 + (\omega\tau)^2)^{-1}$ of the susceptibility dissipative component was retrieved from SAR results. This factor shows a sharp maximum at $D \sim 16\,\text{nm}$. This maximum corresponds to the resonant size of our MNPs for the working frequency of $2.6 \times 10^5\,\text{Hz}$. The relaxation time τ values obtained from the frequency factor compare satisfactorily with those calculated for the Néel and Brown moment relaxation mechanisms. The analysis is consistent with the existence of a crossover from the Néel to Brown mechanisms at $D \sim 18\,\text{nm}$.

Our analysis leads us to the conclusion that to improve SAR performance of magnetite-based materials it is necessary to enhance M_s and K by doping at the optimum level while keeping D around the resonant size corresponding to the working frequency.

Acknowledgments

The authors appreciate P Bercoff for magnetic measurements and financial support by LNLS synchrotron, Campinas-SP, Brazil (proposals D04B-XAFS1 9187/09 and D04B-XAFS1–8625/09), CONICET, Argentina (PIPs 6011 and 0111), ANPCYT, Argentina (PICTs 12-14526 and 03-00898) and RN3M, Argentina.

References

Ammar S, Jouini N, Fiévet F, Stephan O, Marhic C, Richard M, Villain F, Cartier dit Moulin Ch, Brice S and Sainctavit 2004 *J. Non-Crystal. Solids* **345&346** 658–62
Behdadfar B, Kermanpur A, Sadeghi-Aliabadi H, Morales M P and Mozaffari M 2012 *J. Magn. Magn. Mater.* **324** 2211–7
Brezovich I A 1987 *Biological, Physical and Clinical Aspects of Hyperthermia* ed B R Paliwal *et al* (*Medical Physics Monograph* No 16) (New York: AIP) pp 82–110
Carrey J, Mehdaoui B and Respaud M 2011 *J. Appl. Phys.* **109** 083921
Chikazumi S 1964 *Physics of Magnetism* (New York: Wiley) p 100
Cullity B D and Graham C D 2009 *Introduction to Magnetic Materials* (New York: Wiley) p 388
de Paula L B, Primo F L, Jardim D R, Morais P C and Tedesco A C 2012 *J. Appl. Phys.* **111** 07B307
Fiorani D, Testa A M, Lucari F, D'Orazio F and Romero H 2002 *Physica* B **320** 122–6
Fortin J-P, Gazeau F and Wilhelm C 2008 *Eur. Biophys. J.* **37** 223–8
Gneveckow U, Jordan A, Scholz R, Brüß V, Waldöfner N, Ricke J, Feussner A, Hildebrandt B, Rau B and Wust P 2004 *Med. Phys.* **31** 1444–51
Häfeli U O, Aue J and Damani J 2007 The biocompatibility and toxicity of magnetic particles *Magnetic Cell Separation* ed M Zborowski and J J Chalmers (Amsterdam: Elsevier) pp 163–223
Hergt R, Hiergeist R, Zeisberger M, Schüler D, Heyen U, Hilger I and Kaiser W A 2005 *J. Magn. Magn. Mater.* **293** 80–6
Hergt R, Dutz S, Müller R and Zeisberger M 2006 *J. Phys.: Condens. Matter* **18** S2919–34
Kaiser R and Miskolczy G 1970 *J. Appl. Phys.* **41** 1064–72
Kim D K, Zhang Y, Voit W, Rao K V and Muhammed M 2001 *J. Magn. Magn. Mater.* **225** 30–6
Knobel M, Nunes W C, Socolovsky L M, De Biasi E, Vargas J M and Denardin J C 2008 *J. Nanosci. Nanotechnol.* **8** 2836–57
Lutterotti L 2010 *Nucl. Instrum. Methods Phys. Res.* B **268** 334–40
Maier-Hauff K, Ulrich F, Nestler D, Niehoff H, Wust P, Thiesen B, Orawa H, Budach V and Jordan A 2011 *J. Neurooncol.* **103** 317–24
Nakashima S, Fujita K, Tanaka K, Hirao K, Yamamoto T and Tanaka I 2007 *Phys. Rev.* B **75** 174443
Overggard J 1989 *Int. J. Radiat. Oncol. Biol. Phys.* **16** 535–49
Pankhurst Q A, Thanh N K T, Jones S K and Dobson J 2009 Progress in applications of magnetic nanoparticles in biomedicine *J. Phys. D: Appl. Phys.* **42** 224001
Ravel B and Newville M 2005 *J. Synchrotron Radiat.* **12** 537–41
Ren Y *et al* 2012 *Int. J. Nanomed.* **7** 2261–9
Rosensweig R E 2002 *J. Magn. Magn. Mater.* **252** 370–4
Smith D O 1956 *Phys. Rev.* **102** 959–63
Sorensen C M 2001 *Nanoscale Materials in Chemistry* ed K J Klabunde (New York: Wiley) p 169
Stewart S J, Figueroa S J A, Ramallo López J M, Marchetti S G, Bengoa J F, Prado R J and Requejo F G 2007 *Phys. Rev.* B **75** 073408
Tasaki J and Izushi T 1977 *J. Physique Colloque* C1 (suppl. 4) **38** C1-175
Vandenberghe R E and de Grave E 1989 Mössbauer effect studies of oxidic spinels *Mössbauer Spectroscopy Applied to Inorganic Chemistry* vol 3 ed G J Long and F Grandjean (New York: Plenum) pp 59–182
Vandenberghe R E, Barrero C A, Da Costa G M, Van San E and De Grave E 2000 *Hyperfine Interactions* **126** 247–59
Vergés M A, Costo R, Roca A G, Marco J F and Goya G F 2008 *J. Phys. D: Appl. Phys.* **41** 134003
Wen M, Li Q and Li Y 2006 *J. Electron Spectrosc. Relat. Phenom.* **153** 65–70